Inorg. Chem. **2005**, *44*, 9322–9334

Computational Studies of the H-Cluster of Fe-Only Hydrogenases: Geometric, Electronic, and Magnetic Properties and Their Dependence on the [Fe_4S_4] Cubane

Adam T. Fiedler and Thomas C. Brunold*

Department of Chemistry, University of Wisconsin—Madison, 1101 West University Avenue, Madison, Wisconsin 53706

Received June 11, 2005

The active sites of Fe-only hydrogenases (FeHases) feature an unusual polynuclear iron–sulfur cluster, known as the H-cluster, that consists of a [Fe_4S_4] cubane linked to a di-iron subunit (the $[2Fe]_H$ component) via a bridging cysteine ligand (S_{Cys}). While previous computational studies of FeHases employed H-cluster models that only included the $[2Fe]_H$ component, we have utilized density functional theory (DFT), in conjunction with the broken-symmetry (BS) approach, to explore the geometric, electronic, and magnetic properties of the *entire* H-cluster. These calculations have allowed us to evaluate, for the first time, the influence of the [Fe_4S_4] cubane on the $[2Fe]_H$ component of the H-cluster in its active ($\mathbf{H_{ox}}$) and CO-inhibited ($\mathbf{H_{ox}}$**-CO**) states, both of which are paramagnetic ($S = {}^1/_2$). Our results reveal that the presence of the cubane tunes both the position and the donor strength of the S_{Cys} ligand, which, in turn, modulates the internal geometric and electronic structures of the $[2Fe]_H$ subcluster. Importantly, the BS methodology provides an accurate description of the exchange interactions within the H-cluster, permitting insight into the electronic origin of the changes in magnetic properties observed experimentally upon conversion of $\mathbf{H_{ox}}$ to $\mathbf{H_{ox}}$**-CO**. Specifically, while the unpaired spin density in the $\mathbf{H_{ox}}$ state is localized on the distal Fe center, in the $\mathbf{H_{ox}}$**-CO** state, it is delocalized over the $[2Fe]_H$ component, such that the proximal Fe center acquires significant spin density (where distal and proximal refer to the positions of the Fe centers relative to the cubane). To validate our H-cluster models on the basis of experimental data, two DFT-based approaches and the semiempirical INDO/S method have been employed to compute electron paramagnetic resonance parameters for the H-cluster states. While most computations yield reasonably accurate *g* values and ligand hyperfine coupling constants (i.e., *A* values) for the $\mathbf{H_{ox}}$ and $\mathbf{H_{ox}}$**-CO** states, they fail to reproduce the isotropic ^{57}Fe **A** tensors found experimentally. Finally, extension of the computational methodology employed successfully for the $\mathbf{H_{ox}}$ and $\mathbf{H_{ox}}$**-CO** states to the metastable $\mathbf{H_{ox}^{photo}}$ state, generated by irradiation of the $\mathbf{H_{ox}}$**-CO** state at cryogenic temperatures, has allowed us to discriminate between proposed structural models for this species.

Introduction

Hydrogenases are a family of enzymes found in microbial organisms that catalyze the consumption and production of molecular hydrogen via the reversible reaction[2,3]

$$H_2 \leftrightarrows 2H^+ + 2e^- \quad (1)$$

Of the three classes of hydrogenases known to date, the most abundant are the [NiFe] hydrogenases that feature a heterobimetallic [NiFe] cluster at the active site.[4] Although less widespread, the Fe-only hydrogenases (FeHases)[1] have also attracted a great deal of interest because of the presence of an unusual 6-Fe cluster (the H-cluster) that serves as the site of dihydrogen activation and/or production. The most commonly studied FeHases are obtained from the sulfate-

* To whom correspondence should be addressed. E-mail: brunold@chem.wisc.edu.

(1) Abbreviations used: ADF, Amsterdam density functional; AF, antiferromagnetic; BS, broken symmetry; CI, configuration interaction; CP-SCF, coupled−perturbed self-consistent field; DFT, density functional theory; ENDOR, electron nuclear double resonance; EPR, electron paramagnetic resonance; F, ferromagnetic; FeHase, Fe-only hydrogenase; FTIR, Fourier transform infrared; HOMO, highest-occupied molecular orbital; HS, high spin; INDO/S, intermediate neglect of differential overlap, spectroscopic parametrization; HOMO, highest occupied molecular orbital; LS, low spin; LUMO, lowest unoccupied molecular orbital; MO, molecular orbital; pdt, propanedithiolate; SOC, spin−orbit coupling; SOMO, singly occupied molecular orbital; ZORA, zeroth-order regular approximation.

10.1021/ic050946f CCC: $30.25
Published on Web 11/10/2005

Chart 1. FeHase H-Cluster Structure

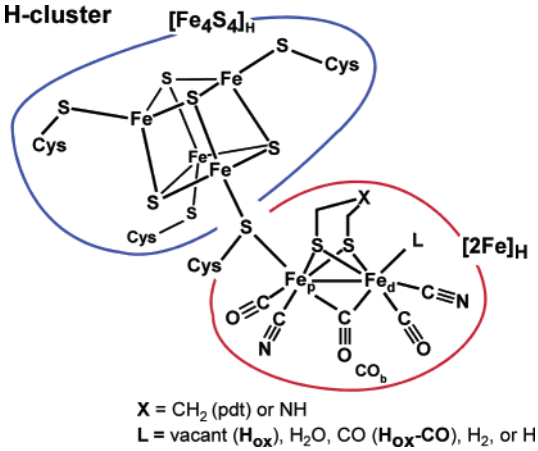

reducing *Desulfovibrio vulgaris* (*Dv*)[5] and the fermentative *Clostridium pasteurianum* (*Cp*) species.[6] The *Cp* organism contains two distinct FeHases, *Cp*I and *Cp*II; the former catalyzes both the forward and back reactions of eq 1 (bidirectional hydrogenase), whereas the latter functions only in the oxidation of H_2 (forward reaction of eq 1; uptake hydrogenase).[3,6] Along with the catalytic clusters, the [NiFe] hydrogenases and FeHases also possess "conventional" $[Fe_2S_2]$ and $[Fe_4S_4]$ clusters, with the number and types of these clusters varying among FeHases.[3] It is believed that these additional Fe/S clusters function in electron transfer to and from the active site.

X-ray crystallographic studies of FeHases from *Cp*[7] and *Desulfovibrio desulfuricans* (*Dd*)[8] have revealed that the H-cluster consists of a $[Fe_4S_4]$ cubane linked to a 2-Fe subcluster (hereafter referred to as the $[2Fe]_H$ component).[9] As illustrated in Chart 1, each Fe atom within this subcluster is coordinated by terminal CN and CO ligands,[10] and the two metal centers are bridged by an exogenous dithiolate moiety believed to be either propanedithiolate (pdt) or di-(thiomethyl)amine (X = CH_2 or NH, respectively, in Chart 1).[8,11] An additional CO ligand (CO_b) occupies a position between the Fe centers. The coordination sphere of the "proximal" Fe (Fe_p) is completed by a cysteine (Cys) linkage to the $[Fe_4S_4]_H$ cubane, while the "distal" Fe (Fe_d) has a labile coordination site (L) that is the putative site of H_2 binding during catalysis (Chart 1). The short Fe−Fe distance of 2.6 Å in the $[2Fe]_H$ component indicates the presence of a strong metal−metal bond.[7]

FeHases have been studied extensively by a variety of spectroscopic techniques, including electron paramagnetic resonance (EPR),[6,12−15] electron nuclear double resonance (ENDOR),[15,16] magnetic circular dichroism (MCD),[13,17] Mössbauer,[16,18−20] resonance Raman,[21] and Fourier transform infrared (FTIR).[10,11,22] Of these techniques, EPR spectroscopy has played a particularly important role in identifying and characterizing the multiple oxidation states of the H-cluster. Table 1 summarizes the magnetic parameters determined for the H-clusters of *Dv*H, *Cp*I, and *Cp*II in their paramagnetic states. The catalytically active form of the H-cluster is the paramagnetic ($S = {}^1/_2$) $\mathbf{H_{ox}}$ state, which exhibits a rhombic EPR signal for all FeHases. Treatment of the $\mathbf{H_{ox}}$ species with CO, a potent inhibitor of FeHases, gives rise to axial EPR signals for *Cp*I and *Dv*H, while a more rhombic spectrum with less dispersed g values is observed for the $\mathbf{H_{ox}}$**-CO** state of *Cp*II (Table 1). Crystallographic studies[23,24] have concluded that the added CO binds to the labile site (L) of the $[2Fe]_H$ component (Chart 1), which is likely vacant in the $\mathbf{H_{ox}}$ state. Interestingly, irradiation of the CO-treated enzyme at low temperatures can produce a distinct species

(2) (a) Armstrong, F. A. *Curr. Opin. Chem. Biol.* **2004**, *8*, 133−140. (b) Evans, D. J.; Pickett, C. J. *Chem. Soc. Rev.* **2003**, *32*, 268−275.
(3) (a) Adams, M. W. W.; Stiefel, E. I. *Curr. Opin. Chem. Biol.* **2000**, *4*, 214−220. (b) Adams, M. W. W. *Biochim. Biophys. Acta* **1990**, *1020*, 115−145.
(4) Volbeda, A.; Fontecilla-Camps, J. C. *J. Chem. Soc., Dalton Trans.* **2003**, 4030−4038.
(5) Huynh, B. H.; Czechowski, M. H.; Kruger, H. J.; Dervartanian, D. V.; Peck, H. D.; Legall, J. *Proc. Natl. Acad. Sci. U.S.A.* **1984**, *81*, 3728−3732.
(6) Adams, M. W. W.; Mortenson, L. E. *J. Biol. Chem.* **1984**, *259*, 7045−7055.
(7) Peters, J. W.; Lanzilotta, W. N.; Lemon, B. J.; Seefeldt, L. C. *Science* **1998**, *282*, 1853−1858.
(8) Nicolet, Y.; Piras, C.; Legrand, P.; Hatchikian, C. E.; Fontecilla-Camps, J. C. *Structure* **1999**, *7*, 13−23.
(9) (a) Nicolet, Y.; Lemon, B. J.; Fontecilla-Camps, J. C.; Peters, J. W. *Trends Biochem. Sci.* **2000**, *25*, 138−143. (b) Peters, J. W. *Curr. Opin. Struct. Biol.* **1999**, *9*, 670−676.
(10) (a) de Lacey, A. L.; Stadler, C.; Cavazza, C.; Hatchikian, E. C.; Fernandez, V. M. *J. Am. Chem. Soc.* **2000**, *122*, 11232−11233. (b) Pierik, A. J.; Hulstein, M.; Hagen, W. R.; Albracht, S. P. J. *Eur. J. Biochem.* **1998**, *258*, 572−578.
(11) Nicolet, Y.; de Lacey, A. L.; Vernede, X.; Fernandez, V. M.; Hatchikian, E. C.; Fontecilla-Camps, J. C. *J. Am. Chem. Soc.* **2001**, *123*, 1596−1601.
(12) (a) Bennett, B.; Lemon, B. J.; Peters, J. W. *Biochemistry* **2000**, *39*, 7455−7460. (b) Pierik, A. J.; Hagen, W. R.; Redeker, J. S.; Wolbert, R. B. G.; Boersma, M.; Verhagen, M.; Grande, H. J.; Veeger, C.; Mutsaers, P. H. A.; Sands, R. H.; Dunham, W. R. *Eur. J. Biochem.* **1992**, *209*, 63−72. (c) Patil, D. S.; Moura, J. J. G.; He, S. H.; Teixeira, M.; Prickril, B. C.; Dervartanian, D. V.; Peck, H. D.; Legall, J.; Huynh, B. H. *J. Biol. Chem.* **1988**, *263*, 18732−18738. (d) Patil, D. S.; Huynh, B. H.; He, S. H.; Peck, H. D.; Dervartanian, D. V.; Legall, J. *J. Am. Chem. Soc.* **1988**, *110*, 8533−8534. (e) Adams, M. W. W. *J. Biol. Chem.* **1987**, *262*, 15054−15061.
(13) Zambrano, I. C.; Kowal, A. T.; Mortenson, L. E.; Adams, M. W. W.; Johnson, M. K. *J. Biol. Chem.* **1989**, *264*, 20974−20983.
(14) Kowal, A. T.; Adams, M. W. W.; Johnson, M. K. *J. Biol. Chem.* **1989**, *264*, 4342−4348.
(15) (a) Telser, J.; Benecky, M. J.; Adams, M. W. W.; Mortenson, L. E.; Hoffman, B. M. *J. Biol. Chem.* **1987**, *262*, 6589−6594. (b) Telser, J.; Benecky, M. J.; Adams, M. W. W.; Mortenson, L. E.; Hoffman, B. M. *J. Biol. Chem.* **1986**, *261*, 3536−3541.
(16) Wang, G.; Benecky, M. J.; Huynh, B. H.; Cline, J. F.; Adams, M. W. W.; Mortenson, L. E.; Hoffman, B. M.; Munck, E. *J. Biol. Chem.* **1984**, *259*, 4328−4331.
(17) (a) Adams, M. W. W.; Johnson, M. K.; Zambrano, I. C.; Mortenson, L. E. *Biochimie* **1986**, *68*, 35−41. (b) Thomson, A. J.; George, S. J.; Richards, A. J. M.; Robinson, A. E.; Grande, H. J.; Veeger, C.; Vandijk, C. *Biochem. J.* **1985**, *227*, 333−336. (c) Stephens, P. J.; Devlin, F.; McKenna, M. C.; Morgan, T. V.; Czechowski, M.; Dervartanian, D. V.; Peck, H. D.; Legall, J. *FEBS Lett.* **1985**, *180*, 24−28.
(18) Pereira, A. S.; Tavares, P.; Moura, I.; Moura, J. J. G.; Huynh, B. H. *J. Am. Chem. Soc.* **2001**, *123*, 2771−2782.
(19) Popescu, C. V.; Munck, E. *J. Am. Chem. Soc.* **1999**, *121*, 7877−7884.
(20) Rusnak, F. M.; Adams, M. W. W.; Mortenson, L. E.; Munck, E. *J. Biol. Chem.* **1987**, *262*, 38−41.
(21) (a) Fu, W.; Drozdzewski, P. M.; Morgan, T. V.; Mortenson, L. E.; Juszczak, A.; Adams, M. W. W.; He, S. H.; Peck, H. D.; Dervartanian, D. V.; Legall, J.; Johnson, M. K. *Biochemistry* **1993**, *32*, 4813−4819. (b) Macor, K. A.; Czernuszewicz, R. S.; Adams, M. W. W.; Spiro, T. G. *J. Biol. Chem.* **1987**, *262*, 9945−9947.
(22) Chen, Z. J.; Lemon, B. J.; Huang, S.; Swartz, D. J.; Peters, J. W.; Bagley, K. A. *Biochemistry* **2002**, *41*, 2036−2043.
(23) Lemon, B. J.; Peters, J. W. *J. Am. Chem. Soc.* **2000**, *122*, 3793−3794.
(24) Lemon, B. J.; Peters, J. W. *Biochemistry* **1999**, *38*, 12969−12973.

Table 1. Summary of FeHase Spectroscopic Data

state	enzyme	*g* values g_1	g_2	g_3	ref
$\mathbf{H_{ox}}$	*Cp*I	2.098	2.040	2.001	12e
	*Cp*II	2.078	2.027	1.999	12e
	*Dv*H	2.100	2.040	2.000	12c
$\mathbf{H_{ox}}$**-CO**	*Cp*I	2.074	2.011	2.011	12e
	CpII	2.032	2.017	1.998	12e
	*Dv*H	2.060	2.010	2.010	12d
$\mathbf{H_{ox}^{photo}}$	*Cp*I	2.260	2.120	1.890	14

state	enzyme	isotropic ^{57}Fe *A* values (MHz) $[Fe_4S_4]_H$	$[2Fe]_H$	ref
$\mathbf{H_{ox}}$	*Cp*I	$\|A_1\| = \|A_2\| = 9.5$	$A_3 = -17.0$	16
	*Cp*II	$\|A_1\| = \|A_2\| = 7.5$	$A_3 = -18.0$	19
	*Dv*H	$\|A_1\| = \|A_2\| = 6.2$	$A_3 = -12.0$	18
$\mathbf{H_{ox}}$**-CO**	*Cp*I	$\|A_1\| = \|A_2\| = 30-34$	$A_3 = -6.0$	15b
	*Cp*II	$A_1 = +25.3, A_2 = -28.3$	$A_3 = -9.5$	19
	*Dv*H	$A_1 = +21.6, A_2 = -24.7$	$A_3 = -5.0$	18

($\mathbf{H_{ox}^{photo}}$) with a highly rhombic EPR signal (Table 1).[14] Although the exact nature of this unstable form of the H-cluster is not known, FTIR studies have suggested that it may result from photodissociation of the bridging CO ligand.[22] Finally, treatment of FeHases with dithionite produces the EPR-silent $\mathbf{H_{red}}$ state.[20] FTIR and crystallographic studies have revealed that the bridging carbonyl in the $\mathbf{H_{red}}$ state is shifted toward Fe_d to generate a terminal CO_b ligand.[11]

Mössbauer studies have demonstrated that the $[Fe_4S_4]_H$ cubane of the H-cluster remains in its oxidized (2+) state in all well-characterized forms of the H-cluster ($\mathbf{H_{ox}}$, $\mathbf{H_{ox}}$**-CO**, and $\mathbf{H_{red}}$), indicating that changes in oxidation state occur only at the $[2Fe]_H$ component of the H-cluster.[18,19] However, although the $[Fe_4S_4]_H$ cluster is formally in its diamagnetic 2+ state, Mössbauer and ENDOR studies have shown that the four Fe sites of the cubane display certain paramagnetic features, as manifested by the ^{57}Fe hyperfine coupling parameters (*A* values).[15,18,19] For the $\mathbf{H_{ox}}$ state, the magnitude of this $[Fe_4S_4]_H$ hyperfine coupling is $A = 5-10$ MHz, which greatly increases to $A = 20-35$ MHz upon conversion to the $\mathbf{H_{ox}}$**-CO** state (see Table 1 for a more detailed summary of H-cluster hyperfine coupling constants). The apparent paramagnetism of the $[Fe_4S_4]_H$ cluster arises from exchange coupling between the cubane and the $[2Fe]_H$ component via the bridging Cys residue, which permits spin delocalization from the $[2Fe]_H$ site onto the cubane.[18,19]

The oxidation states of the Fe atoms in the $[2Fe]_H$ component could not be determined conclusively by Mössbauer spectroscopy,[25] and it has thus been a matter of dispute whether the $2e^-$ catalytic mechanism of FeHases involves an $Fe^{3+}-Fe^{3+} \leftrightarrow Fe^{2+}-Fe^{2+}$ cycle or an $Fe^{2+}-Fe^{2+} \leftrightarrow Fe^{+}-Fe^{+}$ cycle, although a recent computational study has favored the latter scenario.[26] The ability of the H-cluster to access the Fe^+ state, which has no precedent in biological systems, was further supported by the synthesis of binuclear Fe^+-Fe^+ dimer complexes that accurately model the structure and reactivity of the $\mathbf{H_{red}}$ state of the $[2Fe]_H$ subcluster.[27,28] In light of these results, the prevailing mechanism is that the $\mathbf{H_{ox}}$ and $\mathbf{H_{ox}}$**-CO** signals arise from a mixed-valence $Fe^{2+}-Fe^+$ state, although the extent of electron localization remains poorly understood. These low Fe oxidation states in the $[2Fe]_H$ subcluster also seem feasible considering the presence of numerous strong-field CO and CN ligands.

In recent years, several computational studies of FeHases have been carried out.[26,29−31] These studies have provided detailed insight into the geometry and energetics of the $[2Fe]_H$ component in the various H-cluster oxidation states, as well as potential intermediates in the catalytic cycle. However, all theoretical investigations of the H-cluster performed to date[32] have omitted the $[Fe_4S_4]_H$ cubane and instead modeled its presence by varying the protonation state of the Cys residue coordinated to the Fe_p center. While this approach may be justified by the fact that the $[2Fe]_H$ subunit is the likely site of H_2 uptake/formation, it is important to note that, as mentioned above, the $[Fe_4S_4]_H^{2+}$ cubane acquires weak paramagnetism in the $\mathbf{H_{ox}}$ and $\mathbf{H_{ox}}$**-CO** states through exchange interactions with the $[2Fe]_H$ subcluster, indicating a significant degree of electronic communication between the two units. Moreover, it is likely that the $[Fe_4S_4]_H$ cubane influences the geometric and electronic structures of the $[2Fe]_H$ component. The challenge in treating the entire H-cluster with computational methods lies in the exchange interactions among the multiple Fe centers. Such spin-coupled systems are difficult to treat with density functional theory (DFT) in particular because their ground-state wave functions typically correspond to linear combinations of multiple determinants, while DFT calculations are limited to single-determinant wave functions. However, exchange interactions within metal clusters can be treated reasonably well with DFT by employing the broken-symmetry (BS) methodology pioneered by Noodleman and co-workers.[33]

(25) Although the Fe isomer shift (δ) is typically a reliable indicator of oxidation state, the δ values of LS Fe atoms ligated by CO and CN^- ligands are largely insensitive to changes in oxidation state.[18,19]

(26) Cao, Z. X.; Hall, M. B. *J. Am. Chem. Soc.* **2001**, *123*, 3734−3742.

(27) (a) Schmidt, M.; Contakes, S. M.; Rauchfuss, T. B. *J. Am. Chem. Soc.* **1999**, *121*, 9736−9737. (b) Lyon, E. J.; Georgakaki, I. P.; Reibenspies, J. H.; Darensbourg, M. Y. *Angew. Chem., Int. Ed.* **1999**, *38*, 3178−3180.

(28) Le Cloirec, A.; Best, S. P.; Borg, S.; Davies, S. C.; Evans, D. J.; Hughes, D. L.; Pickett, C. J. *Chem. Commun.* **1999**, 2285−2286.

(29) (a) Zhou, T. J.; Mo, Y. R.; Liu, A. M.; Zhou, Z. H.; Tsai, K. R. *Inorg. Chem.* **2004**, *43*, 923−930. (b) Bruschi, M.; Fantucci, P.; De Gioia, L. *Inorg. Chem.* **2003**, *42*, 4773−4781.

(30) (a) Bruschi, M.; Fantucci, P.; De Gioia, L. *Inorg. Chem.* **2004**, *43*, 3733−3741. (b) Bruschi, M.; Fantucci, P.; De Gioia, L. *Inorg. Chem.* **2002**, *41*, 1421−1429. (c) Fan, H. J.; Hall, M. B. *J. Am. Chem. Soc.* **2001**, *123*, 3828−3829.

(31) Liu, Z. P.; Hu, P. *J. Am. Chem. Soc.* **2002**, *124*, 5175−5182.

(32) While this paper was under review, a DFT study was published in which the $[Fe_4S_4]$ cubane was included in some H-cluster models: Zhou, T.; Mo, Y.; Zhou, Z.; Tsai, K. *Inorg. Chem.* **2005**, *44*, 4941−4946. However, Zhou and co-workers acknowledge that their computational approach does not treat the electronic structure of the cubane in a realistic manner because all spin-coupling and polarization effects within the cluster were ignored. Consequently, this study provides only limited insight into the effects of the $[Fe_4S_4]_H$ cubane on the geometric and electronic structures of the $[2Fe]_H$ component.

(33) (a) Noodleman, L.; Lovell, T.; Liu, T. Q.; Himo, F.; Torres, R. A. *Curr. Opin. Chem. Biol.* **2002**, *6*, 259−273. (b) Noodleman, L.; Peng, C. Y.; Case, D. A.; Mouesca, J. M. *Coord. Chem. Rev.* **1995**, *144*, 199−244. (c) Noodleman, L.; Case, D. A. *Adv. Inorg. Chem.* **1992**, *38*, 423−470.

In a previous computational study, we successfully applied the BS-DFT methodology to the A-cluster of acetyl coenzyme-A synthase, which, like the H-cluster, features a $[Fe_4S_4]$ cubane linked to a bimetallic fragment.[34] In this study, a similar approach was used to carry out the first computational investigation of the H-cluster in its entirety. These "6-Fe" model calculations allowed us to examine the role of the $[Fe_4S_4]_H$ cubane in modulating the structure and bonding of the $[2Fe]_H$ component. Additionally, we were able to calculate the magnitude of the exchange interaction between the two subclusters, which provides a direct measure of the distribution of unpaired spin density within the $[2Fe]_H$ unit in the paramagnetic states. With the $[2Fe]_H$ geometries provided by these 6-Fe model calculations, we then utilized recently developed DFT approaches to compute relevant EPR parameters for the $\mathbf{H_{ox}}$ and $\mathbf{H_{ox}}$**-CO** states, so as to provide a further link between our computational results and experimental data. Collectively, the results obtained in this study provide significant new insights into the relationships between the geometric structure, electronic properties, and magnetic parameters of the H-cluster, as well as the structure of the cluster in the $\mathbf{H_{ox}^{photo}}$ state.

Computational Methodology

1. Computational Details. H-cluster models were generated by constrained DFT geometry optimizations using the Amsterdam Density Functional (ADF) software package.[35] Initial structures for these optimizations were derived from published X-ray crystallographic data of *Cp*I.[7,36] The bridging dithiolate ligand was modeled as a pdt moiety in all structures. The Cys residues were truncated to methyl thiolate (CH_3S^-) ligands, and the carbon atoms of these ligands were fixed at their crystallographically determined positions. All optimizations were carried out on a cluster of 20 Intel Xeon processors (Ace computers) using an integration constant of 4.0 and the Vosko−Wilk−Nusair local density approximation,[37] along with the nonlocal gradient corrections of Becke[38] and Perdew.[39] Relativistic effects were incorporated with the scalar zeroth-order regular approximation (ZORA) Hamiltonian.[40] A ZORA verison of ADF basis set IV (triple-ζ with single polarization) that includes steeper core functions was utilized, and all electrons were explicitly included in the calculations (i.e., no use was made of the frozen-core approximation). The Cartesian coordinates for all DFT geometry-optimized models mentioned in the text are available in the Supporting Information (Table S4a−g).

Single-point DFT calculations were also performed using the ORCA 2.2 software package developed by Neese.[41] These computations utilized Ahlrichs' valence triple-ζ basis set[42] with two sets of polarization functions[43] (VTZ/PP) on Fe and S and one set of polarization functions on all other atoms, in conjunction with the corresponding auxiliary basis set.[44] All calculations were carried out with an integration grid of 4.0 and employed Becke's three-parameter hybrid functional[45] for exchange along with the Lee−Yang−Parr correlation functional[46] (B3LYP). The gOpenMol program[47] developed by Laaksonen was used to generate isosurface plots of molecular orbitals (MOs; using an isodensity value of 0.05 au).

EPR parameters (**g** and **A** tensors) were computed with two distinct DFT methodologies, as implemented in ADF and ORCA. In the former method, the **g** tensor was derived from a spin-restricted wave function that accounted for spin−orbit coupling (SOC) via the ZORA Hamiltonian.[48] This calculation also provided the anisotropic components of the **A** tensors, while the corresponding isotropic parameters (A_{iso}) were obtained from an unrestricted calculation that accounted for spin polarization at the nuclei.[49] These calculations employed the same all-electron basis sets and functionals described above for the geometry optimizations. In the ORCA calculations, the contribution of SOC to the **g** and **A** tensors was evaluated by solving the coupled−perturbed self-consistent field (CP-SCF) equations,[50] which employ the parametrization of Koseki and co-workers.[51] The B3LYP

(34) Schenker, R. P.; Brunold, T. C. *J. Am. Chem. Soc.* **2003**, *125*, 13962−13963.

(35) (a) Baerends, E. J.; Ellis, D. E.; Ros, P. *Chem. Phys.* **1973**, *2*, 41. (b) Guerra, C. F.; Snijders, J. G.; te Velde, G.; Baerends, E. J. *Theor. Chem. Acc.* **1998**, *99*, 391−403. (c) te Velde, G.; Baerends, E. J. *J. Comput. Phys.* **1992**, *99*, 84−98. (d) Versluis, L.; Ziegler, T. *J. Chem. Phys.* **1988**, *88*, 322−328.

(36) The H-cluster structure reported in ref 7 contains a H_2O molecule at the labile coordination site of Fe_d. However, previous computational studies[26,31] have indicated that this site is vacant in the $\mathbf{H_{ox}}$ state, and our $\mathbf{H_{ox}}$ models therefore omit the H_2O ligand. The crystallographically derived H-cluster structures likely reflect a mixture of oxidation states, and the aforementioned computational studies have suggested that the fully oxidized EPR-silent state (i.e., one-electron oxidized relative to $\mathbf{H_{ox}}$) may bind a H_2O molecule at Fe_d.

(37) Vosko, S. H.; Wilk, L.; Nusair, M. *Can. J. Phys.* **1980**, *58*, 1200−1211.

(38) Becke, A. D. *J. Chem. Phys.* **1986**, *84*, 4524−4529.

(39) Perdew, J. P. *Phys. Rev. B: Condens. Matter* **1986**, *33*, 8822−8824.

(40) (a) van Lenthe, E.; Ehlers, A.; Baerends, E. J. *J. Chem. Phys.* **1999**, *110*, 8943−8953. (b) van Lenthe, E.; Baerends, E. J.; Snijders, J. G. *J. Chem. Phys.* **1994**, *101*, 9783−9792. (c) van Lenthe, E.; Baerends, E. J.; Snijders, J. G. *J. Chem. Phys.* **1993**, *99*, 4597−4610.

(41) Neese, F. *ORCA, an ab initio, density functional, and semiempirical program package*, version 2.2; Max-Plack Institut für Bioanorganische Chemie: Mülheim an der Ruhr, Germany, 2001.

(42) Schaefer, A.; Horn, H.; Ahlrichs, R. *J. Chem. Phys.* **1992**, *97*, 2571.

(43) Ahlrichs, R. Unpublished results.

(44) (a) Eichkorn, K.; Treutler, O.; Ohm, H.; Haser, M.; Ahlrichs, R. *Chem. Phys. Lett.* **1995**, *240*, 283. (b) Eichkorn, K.; Weigend, F.; Treutler, O.; Ahlrichs, R. *Theor. Chem. Acc.* **1997**, *97*, 119.

(45) Becke, A. D. *J. Chem. Phys.* **1993**, *98*, 1372−1377.

(46) Lee, C. T.; Yang, W. T.; Parr, R. G. *Phys. Rev. B* **1988**, *37*, 785−789.

(47) (a) Bergman, D. L.; Laaksonen, L.; Laaksonen, A. *J. Mol. Graphics Modell.* **1997**, *15*, 301. (b) Laaksonen, L. *J. Mol. Graphics* **1992**, *10*, 33.

(48) (a) Stein, M.; van Lenthe, E.; Baerends, E. J.; Lubitz, W. *J. Am. Chem. Soc.* **2001**, *123*, 5839−5840. (b) van Lenthe, E.; Wormer, P. E. S.; van der Avoird, A. *J. Chem. Phys.* **1997**, *107*, 2488−2498.

(49) (a) Stadler, C.; de Lacey, A. L.; Hernandez, B.; Fernandez, V. M.; Conesa, J. C. *Inorg. Chem.* **2002**, *41*, 4417−4423. (b) Stadler, C.; Lacey, A. L.; Montet, Y.; Volbeda, A.; Fontecilla-Camps, J. C.; Conesa, J. C.; Fernandez, V. M. *Inorg. Chem.* **2002**, *41*, 4424−4434. (c) Stein, M.; van Lenthe, E.; Baerends, E. J.; Lubitz, W. *J. Phys. Chem. A* **2001**, *105*, 416−425. (d) van Lenthe, E.; van der Avoird, A.; Wormer, P. E. S. *J. Chem. Phys.* **1998**, *108*, 4783−4796.

(50) (a) Neese, F. *J. Chem. Phys.* **2003**, *118*, 3939−3948. (b) Neese, F. *Curr. Opin. Chem. Biol.* **2003**, *7*, 125−135. (c) Neese, F. *J. Chem. Phys.* **2001**, *115*, 11080−11096. (d) Sinnecker, S.; Slep, L. D.; Bill, E.; Neese, F. *Inorg. Chem.* **2005**, *44*, 2245−2254.

(51) (a) Koseki, S.; Schmidt, M. W.; Gordon, M. S. *J. Phys. Chem.* **1992**, *96*, 10768−10772. (b) Koseki, S.; Gordon, M. S.; Schmidt, M. W.; Matsunaga, M. J. *J. Phys. Chem.* **1995**, *99*, 12764−12772. (c) Koseki, S.; Schmidt, M. W.; Gordon, M. S. *J. Phys. Chem. A* **1998**, *102*, 10430−10435.

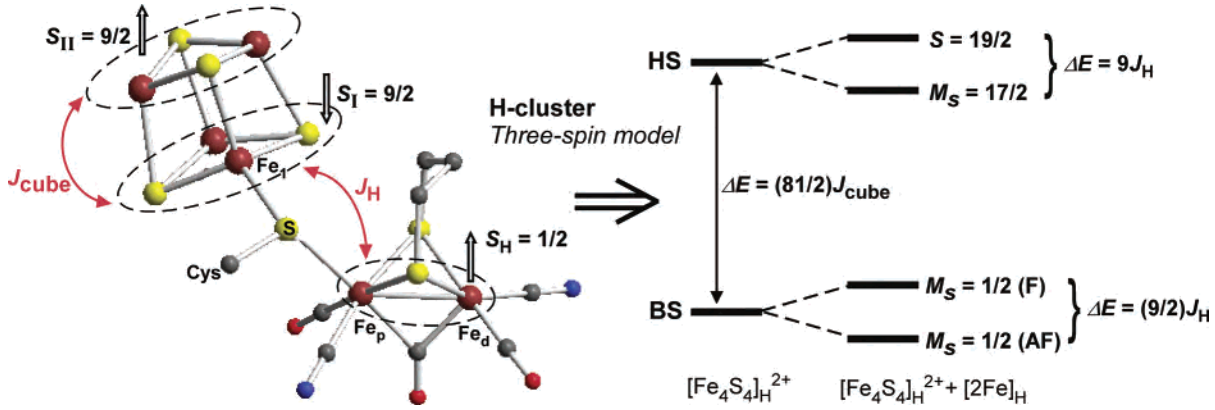

Figure 1. Left: Schematic diagram of the "three-spin model" used to treat the H-cluster. J_{cube} designates the AF exchange interaction between the mixed-valence Fe dimers within the cubane, while J_H is the exchange interaction between the $[2Fe]_H$ component and the adjacent mixed-valence Fe dimer of the $[Fe_4S_4]_H$ cluster. Note that this figure only depicts one of six possible spin-coupling configurations (see text). Right: Spin-state diagram showing how the relative energies of the HS and BS states of the $[Fe_4S_4]_H^{2+}$ cluster are modulated by F and AF interactions with the $S = {}^1/_2$ spin of the $[2Fe]_H$ component.

hybrid functional was used in all cases, along with the "core properties" with extended polarization [CP(PPP)][52] and Kutzelnigg's NMR/EPR (IGLO-III) basis sets[53] to treat the Fe and metal-ligating atoms, respectively. Ahlrichs' VTZ/P basis set[42] was used for all remaining atoms except S, for which an extra polarization function was added. The CP-SCF calculations included all orbitals within a ±100 mhartree window of the highest occupied MO (HOMO)/lowest unoccupied MO (LUMO) energy gap, with the origin of the matrix defined by the center of electronic charge. A high-resolution radial grid with an integration accuracy of 7.0 was used for Fe and relevant ligand atoms.

Semiempirical calculations employing the INDO/S model developed by Zerner and co-workers[54] were also performed using the ORCA program. These calculations used the valence-shell ionization potentials and Slater−Condon parameters listed by Bacon and Zerner[55] and the standard interaction factors $f_{p\sigma p\sigma} = 1.266$ and $f_{p\pi p\pi} = 0.585$. Restricted open-shell Hartree−Fock SCF calculations were converged on the spin doublet ground states of the $[2Fe]_H$ models, which served as the reference states for configuration interaction (CI) calculations. Initial calculations of **g** tensors included single-electron excitations from all doubly occupied MOs (DOMOs) within 5 eV of the HOMO to the singly occupied MO (SOMO) and all virtual MOs within 5 eV of the LUMO, along with double-electron excitations from DOMOs within 2 eV of the HOMO to the SOMO and virtual orbitals within 2 eV of the LUMO. The active space was then expanded in successive calculations until stable results were obtained for the molecular **g** tensor.

2. BS Wave Functions. As noted in the Introduction, the principal challenge in treating the full H-cluster with DFT lies in the exchange interactions that exist between the two subclusters, as well as those within the $[Fe_4S_4]_H$ cubane. Exchange coupling[56] is typically described with the purely phenomenological Heisenberg−Dirac−Van Vleck (HDVV) Hamiltonian: $H = J(\mathbf{S}_A \cdot \mathbf{S}_B)$, where $\mathbf{S}_A$ and $\mathbf{S}_B$ are the spin operators for centers A and B, respectively, and J is the exchange coupling constant. By convention, $J > 0$ for antiferromagnetic (AF) exchange and $J < 0$ for ferromagnetic (F) exchange. When mixed-valence systems are involved, a more complete Hamiltonian that accounts for double exchange is $H = J(\mathbf{S}_A \cdot \mathbf{S}_B) \pm B(S_{total} + {}^1/_2)$, where B is the resonance delocalization parameter.[33]

Even though the cubane itself is diamagnetic, the $[Fe_4S_4]^{2+}$ unit of the H-cluster formally consists of two pairs of high-spin (HS) Fe^{2+} ($S = 2$) and Fe^{3+} ($S = {}^5/_2$) centers. Previous theoretical studies[33,57] have concluded that two exchange phenomena are at work within $[Fe_4S_4]^{2+}$ cubanes: (i) double exchange, which effectively leads to F coupling of the spins for a given pair of Fe centers to yield two dimers with $S = {}^9/_2$, and (ii) Heisenberg exchange, which couples these two $S = {}^9/_2$ dimer spins antiferromagnetically to produce the resulting $S = 0$ ground state. Thus, the H-cluster can be viewed as a three-spin coupling problem with $S_I = S_{II} = {}^9/_2$ and $S_H = {}^1/_2$, where S_I and S_{II} represent the spins of the two mixed-valence Fe dimers that comprise the cubane and S_H represents the spin associated with the $[2Fe]_H$ subunit (Figure 1). This scheme assumes that the double-exchange interactions within the cubane are so strong that the mixed-valence Fe pairs can be treated as a single spin, which is a reasonable assumption on the basis of spectroscopic studies.[58] The three-spin model then requires only two exchange parameters, J_H and J_{cube}, as shown in Figure 1. J_{cube} describes the Heisenberg exchange between the two Fe dimers within the cubane,

(52) Neese, F. *Inorg. Chim. Acta* **2002**, *337*, 181−192.
(53) Kutzelnigg, W.; Fleischer, U.; Schindler, M. *The IGLO Method: Ab Initio Calculation and Interpretation of NMR Chemical Shifts and Magnetic Susceptibilities*; Springer-Verlag: Heidelberg, Germany, 1990; Vol. 23.
(54) (a) Ridley, J.; Zerner, M. C. *Theor. Chem. Acc.* **1973**, *32*, 111. (b) Zerner, M. C.; Loew, G. H.; Kirchner, R. F.; Mueller-Westerhof, U. T. *J. Am. Chem. Soc.* **1980**, *102*, 589.
(55) Bacon, A. D.; Zerner, M. C. *Theor. Chem. Acc.* **1979**, *53*, 21.
(56) (a) Blondin, G.; Girerd, J. J. *Chem. Rev.* **1990**, *90*, 1359−1376. (b) Coronado, E.; Tsukerblat, B. S.; Georges, R. In *Molecular Magnetism: From Molecular Assemblies to Devices*; Coronado, E., Delhaes, P., Gatteschi, D., Miller, J. S., Eds.; Kluwer: Dordrecht, The Netherlands, 1996; pp 65−84.
(57) Bominaar, E. L.; Hu, Z. G.; Munck, E.; Girerd, J. J.; Borshch, S. A. *J. Am. Chem. Soc.* **1995**, *117*, 6976−6989.
(58) (a) Papaefthymiou, V.; Millar, M. M.; Munck, E. *Inorg. Chem.* **1986**, *25*, 3010−3014. (b) Middleton, P.; Dickson, D. P. E.; Johnson, C. E.; Rush, J. D. *Eur. J. Biochem.* **1978**, *88*, 135−141. (c) Cammack, R. *Adv. Inorg. Chem.* **1992**, *38*, 281−322. (d) Middleton, P.; Dickson, D. P. E.; Johnson, C. E.; Rush, J. D. *Eur. J. Biochem.* **1980**, *104*, 289−296.

Table 2. Labels for Computational Models of the H-Cluster

model size	ox state $[Fe_p-Fe_d]^{n+}$	S_{Cys}[a]	H_{ox}	H_{ox}-CO	H_{ox}^{photo} photo-I	H_{ox}^{photo} photo-II
			Optimized Models			
full H-cluster	$n = 3$	S^-	**ox^{6Fe}**	**ox^{6Fe}-CO**	**I^{6Fe}**	**II^{6Fe}**
$[2Fe]_H$ cluster	$n = 3$	SH	**ox^{2Fe}**			
full H-cluster	$n = 5$	S^-	**ox$^{6Fe-high}$**			
$[2Fe]_H$ cluster	$n = 5$	SH	**ox$^{2Fe-high}$**			
			Truncated Models[b]			
$[2Fe]_H$ cluster	$n = 3$	S^-	**ox^{S}**	**ox^{S}-CO**		
$[2Fe]_H$ cluster	$n = 3$	SH	**ox^{SH}**	**ox^{SH}-CO**	**I^{SH}**	**II^{SH}**

[a] Protonation state of the terminal S ligand that coordinates to Fe_p: SH = protonated, S^- = deprotonated. [b] Truncated models were generated from the optimized 6Fe models by removal of the $[Fe_4S_4]_H$ cluster; the models were not further optimized.

whereas J_H corresponds to the exchange between the $[2Fe]_H$ component and the adjacent Fe dimer.[59]

Spin coupling is incorporated into DFT calculations with the construction of BS wave functions, in which the spin-up (α) and spin-down (β) electrons are localized on different parts of the molecule. Although the BS state is not a pure spin state (its wave function is an eigenfunction of M_s, not S^2), it is possible to express the BS wave function as a linear combination of the pure spin-state wave functions with the use of Clebsch−Gordon projection coefficients. Following this approach, Noodleman and co-workers have shown that the coupling constant, J, describing the exchange interaction between two spins (S_A, S_B) can be computed from the energies of the HS and BS states via the following equation:[33]

$$E_{HS}(S_{max} = S_A + S_B) - E_{BS}(M_{BS} = |S_A - S_B|) = 2JS_AS_B \quad (2)$$

For the paramagnetic ($S = {}^1/_2$) states of the H-cluster, the BS wave function ($M_s = {}^1/_2$) is constructed by aligning the $M_s = S_I = S_{II} = {}^9/_2$ spins of the cubane antiferromagnetically, while the $M_s = {}^1/_2$ spin on the $[2Fe]_H$ component remains spin-up. Depending on which Fe centers are paired to yield the mixed-valence dimers, this scheme yields three possible spin configurations for the $[Fe_4S_4]_H^{2+}$ cubane. Each of these spin configurations is then coupled to the spin of the $[2Fe]_H$ component in either a F or AF fashion, resulting in a total of six BS configurations (note that Figure 1 represents only one of these six permutations). The F and AF labels in Figure 1 describe the exchange interaction between the $[2Fe]_H$ cluster and the nearest Fe center of the cubane (Fe_1 in Figure 1). As shown in Figure 1, the energies of the HS ($S = 9$) and BS ($M_s = 0$) states of the $[Fe_4S_4]_H^{2+}$ cluster are split by the interaction with the $S = {}^1/_2$ spin on the $[2Fe]_H$ component, and the magnitude of this splitting is proportional to J_H. Even though eq 2 refers to a two-spin system, it can also be applied to the H-cluster; however, the presence of a third spin does not allow for a unique value. Instead, the splitting of the HS and three BS states leads to four distinct values of J_H, which are obtained from eight separate calculations (six BS + two HS states). Herein, we report the average value of J_H, with the uncertainty provided by the standard deviation of the four values (see Table S2 in the Supporting Information for complete results).

(59) When the mixed-valence Fe pairs are treated as a single spin, this model does not explicitly incorporate the delocalization parameter, B. Moreover, we assume that the interaction between S_H and S_{II} (Figure 1) is negligible. Thus, the two coupling constants, J_H and J_{cube}, are sufficient to model the exchange interactions within the H-cluster.

Results and Analysis

1. H-Cluster Geometries: H_{ox} and H_{ox}-CO. Using the BS methodology described above, constrained DFT geometry optimizations of the complete H-cluster were performed. Calculations of the cluster in the **H_{ox}** and **H_{ox}-CO** states ($M_s = {}^1/_2$) assumed a low-spin (LS) $[Fe-Fe]^{3+}$ oxidation state for the $[2Fe]_H$ subunit, although higher oxidations states were also investigated (vide infra). Table 2 provides a summary of the labeling scheme used for the various H-cluster models studied. For both the **H_{ox}** and **H_{ox}-CO** states, changes in the spin configuration of the $[Fe_4S_4]_H$ cubane had minimal effects on the geometry of the $[2Fe]_H$ subcluster, which is nearly identical in all six BS states investigated. In contrast, the geometry of the $[Fe_4S_4]_H^{2+}$ cluster experienced more dramatic changes because bond lengths and angles within the cubane are dependent upon which Fe centers share the double-exchange interactions. The structural parameters for the lowest-energy models obtained for **H_{ox}** and **H_{ox}-CO** are summarized in Table 3.

As shown in Table 3, the optimized structure of the H-cluster in the **H_{ox}** state (model **ox^{6Fe}**) agrees quite well with the crystallographically determined structures from *Cp*I[7,24] and *Dd*H.[8,36,60] Although the Fe−C(O/N) distances differ substantially, the positions of small diatomic ligands are difficult to determine accurately from protein diffraction data, and the computed distances agree nicely with those found in model complexes of $[2Fe]_H$.[27] While the optimized geometries of the H-cluster in the **H_{ox}** and **H_{ox}-CO** states are largely identical with regards to key structural parameters (i.e., the pdt ligand, the terminal CO/CN ligands, and the $[Fe_4S_4]_H$ cluster), it is interesting to note that the addition of CO to the Fe_d atom alters the relative position of the bridging CO (CO_b) ligand. Specifically, this ligand is approximately

(60) In published crystallographic studies of FeHases, the H-cluster oxidation states are somewhat uncertain, and the resulting structures may reflect a mixture of states. Despite this ambiguity, it is generally assumed that the $[Fe_p-Fe_d]_H$ unit is in the 3+ or 4+ oxidation state and that the H-cluster of the *Cp*I structure is more oxidized than that of *Dd*H.[9]

Table 3. Relevant Interatomic Distances (Å) for DFT-Optimized Models of the H-Cluster and Comparison to Crystallographic Data

bond lengths (Å)[a]	X-ray structures[b]			DFT models			
	*Cp*I[c]	*Cp*I + CO[d]	*Dd*H[e]	**ox^{6Fe}**	**ox^{2Fe}**	Δ[f]	**ox^{6Fe}-CO**
			$[2Fe]_H$				
Fe−Fe	2.62	2.60	2.57	2.56	2.55	−0.01	2.71
Fe_p-S_{pdt} (ave)	2.33	2.36	2.30	2.35	2.34	−0.01	2.35
Fe_d-S_{pdt} (ave)	2.33	2.30	2.29	2.31	2.31	0.00	2.34
Fe_p-S_{Cys}	2.38	2.36	2.50	2.38	2.25	**−0.13**	2.63
$Fe-C(O)_t$ (ave)	1.83	1.82	1.75	1.74	1.75	+0.01	1.75
$Fe-C(N)_t$ (ave)			1.86	1.91	1.91	0.00	1.91
$Fe_p-C(O)_b$	2.10	2.12	2.9	2.00	2.09	**+0.09**	1.80
Fe_d-$C(O)_b$	2.04	2.12	2.6	1.89	1.85	**−0.04**	2.25
			$[Fe_4S_4]_H$				
Fe−Fe (ave)	2.72	2.69	2.70	2.70			2.70
$Fe-S_b$ (ave)	2.31	2.31	2.31	2.27			2.27
$Fe-S_{Cys}$(b)	2.32	2.36	2.34	2.35			2.31
$Fe-S_{Cys}$(t) (ave)	2.28	2.28	2.27	2.27			2.26

[a] Abbreviations: S_{pdt} = S of the bridging pdt ligand, S_{Cys} = S of the Cys ligand, t = terminal, b = bridging. [b] In these crystallographic studies of FeHases, the H-cluster oxidation states are somewhat ambiguous; see ref 60. [c] From ref 7. [d] From ref 24. [e] From ref 8. [f] $\Delta = r(\mathbf{ox^{2Fe}}) - r(\mathbf{ox^{6Fe}})$; significant differences are in boldface.

equidistant between the two Fe centers in model **ox^{6Fe}** but shifts strongly toward the Fe_p in **ox^{6Fe}-CO** (Table 3). As a result, the Fe_p-S_{cys} bond distance increases considerably by 0.25 Å due to the strong trans influence of the CO_b ligand. Moreover, the added CO causes an elongation of the Fe−Fe distance by 0.15 Å, although the optimized value of 2.7 Å for **ox^{6Fe}-CO** remains suggestive of an Fe−Fe bond. We note that these structural differences between the **H_{ox}** and **H_{ox}-CO** states are fully consistent with other DFT studies of the $[2Fe]_H$ component.[26,31]

For comparison, we also performed geometry optimizations of only the $[2Fe]_H$ component of the H-cluster in which the $[Fe_4S_4]_H$ cubane was replaced by a proton, an approximation consistently employed in previous DFT studies of the H-cluster.[26,29,31] Because the S_{Cys} ligand in this truncated model no longer occupies a bridging position between two Fe centers, the resulting 2Fe structure in the **H_{ox}** state (model **ox^{2Fe}**) possesses a much shorter Fe_p-S_{Cys} bond (2.25 Å) than that found in the corresponding 6Fe structure (2.38 Å; see Table 3). Significantly, we again observe a strong correlation between the positions of the S_{Cys} and CO_b ligands, with the shorter Fe_p-S_{Cys} bond in **ox^{2Fe}** forcing CO_b to shift away from Fe_p by ~0.10 Å (these changes are highlighted in Table 3). Thus, it appears that an important structural role of the $[Fe_4S_4]_H$ cluster is to lengthen the Fe_p-S_{Cys} bond, which further impacts the Fe_d center by modulating the relative position of the CO_b ligand.

We also performed calculations on the full H-cluster in which a higher oxidation state of $[Fe-Fe]^{5+}$ was assumed for the $[2Fe]_H$ subunit, as this oxidation state assignment also seems consistent with available spectroscopic data.[25] While the structure of the resulting model (**ox$^{6Fe-high}$**) is not dramatically different from that of the more reduced **ox^{6Fe}** model described above (Table S1), analysis of the Mulliken populations revealed that the $[2Fe]_H$ component of **ox$^{6Fe-high}$** is essentially diamagnetic and that the unpaired spin actually resides on the $[Fe_4S_4]_H$ cubane. Thus, the electron configuration of **ox$^{6Fe-high}$** is best described as $[Fe_4S_4]_H^{3+}-[Fe_p^{2+}-Fe_d^{2+}]$, indicating that oxidation of the $[Fe_4S_4]_H^{2+}$ cubane is energetically more favorable than formation of an Fe^{3+} center in the $[2Fe]_H$ component. This result is not surprising as it is well-known that HS Fe^{2+} centers are generally easier to oxidize than LS Fe^{2+} centers. While it was possible to access the $[Fe-Fe]^{5+}$ state if the $[Fe_4S_4]_H$ cluster was not included in the calculation, the resulting structure of the $[2Fe]_H$ component for the **H_{ox}** state (model **ox$^{2Fe-high}$**) is not compatible with the crystallographic data. Specifically, the CO_b ligand of this highly oxidized model does not occupy the bridging position determined experimentally but instead coordinates terminally to Fe_d (Table S1). Thus, in support of previous computational studies on H-cluster models lacking the $[Fe_4S_4]_H$ cluster,[26] our computational results strongly discount an $[Fe-Fe]^{5+}$ oxidation state assignment.

2. Calculation of Exchange Parameters. As discussed in the Computational Methodology section, the three-spin model of the H-cluster requires two exchange parameters, J_{cube} and J_H, where the former represents the exchange interaction between the mixed-valence Fe dimers within the cubane and the latter describes the AF exchange interaction between the $[2Fe]_H$ component and the adjacent mixed-valence Fe dimer of the $[Fe_4S_4]_H$ cluster (Figure 1). With the energies obtained from BS and HS calculations for the full H-cluster, the values of these exchange parameters for the **H_{ox}** and **H_{ox}-CO** states were estimated using eq 2 (Table S2). For both states, our calculations provided a J_{cube} value near 400 cm^{-1}, which is consistent with previous computational[33] and experimental[61] studies of $[Fe_4S_4]^{2+}$ clusters. More significantly, the calculated J_H value of $+15 \pm 10$ cm^{-1} for the **H_{ox}** state agrees remarkably well with the experimentally determined value of ~20 cm^{-1}.[18,19] Furthermore, our calculations accurately reproduce the large increase in J_H upon binding of CO to Fe_d. Again, the computed value of J_H for the **H_{ox}-CO** state (150 ± 50 cm^{-1}) agrees nicely with the experimental value of ~100 cm^{-1} measured for *Cp*II[19] and *Dv*H.[18] Collectively, this remarkable agreement between experimental and computed structural and exchange parameters suggests that our BS-DFT methodology is quite capable of providing reliable geometric and electronic structure descriptions for the full H-cluster.

3. Electronic Structure of H-Cluster Models. While inclusion of the $[Fe_4S_4]_H$ cubane is essential for an accurate computational prediction of the geometric properties and exchange parameters of the H-cluster, smaller models were used to explore the electronic structure and spectroscopic properties of the catalytically relevant $[2Fe]_H$ component in detail. To this end, single-point DFT calculations were performed with the ORCA program that, unlike ADF, permits the use of hybrid DFT functionals, such as B3LYP.

(61) (a) Papaefthymiou, G. C.; Laskowski, E. J.; Frotapessoa, S.; Frankel, R. B.; Holm, R. H. *Inorg. Chem.* **1982**, *21*, 1723−1728. (b) Laskowski, E. J.; Frankel, R. B.; Gillum, W. O.; Papaefthymiou, G. C.; Renaud, J.; Ibers, J. A.; Holm, R. H. *J. Am. Chem. Soc.* **1978**, *100*, 5322−5337. (c) Wong, G. B.; Bobrik, M. A.; Holm, R. H. *Inorg. Chem.* **1978**, *17*, 578−584. (d) Antanaitis, B. C.; Moss, T. H. *Biochim. Biophys. Acta* **1975**, *405*, 262−279.

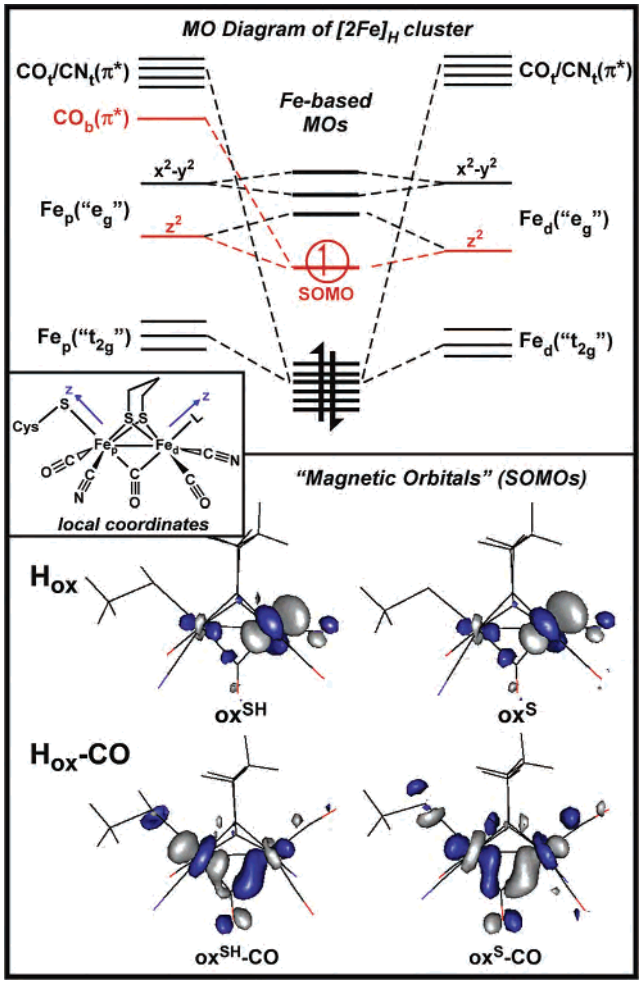

Figure 2. Top: Qualitative MO energy diagram for the $[2Fe]_H$ component based on DFT calculations on the truncated H-cluster models. Only the relative energies of the Fe d-based orbitals are shown for clarity. The orbitals that contribute to the SOMO are highlighted in red. Bottom: Isosurface plots of the SOMOs of the **ox^{SH}, ox^{S}, ox^{SH}-CO,** and **ox^{S}-CO** models from spin-unrestricted DFT computations. Inset: Local coordinate system for the Fe_p and Fe_d centers of the $[2Fe]_H$ component.

To account for the geometric and electronic effects of the $[Fe_4S_4]_H$ cubane, our models of the $[2Fe]_H$ cluster were derived directly from the 6Fe calculations described above and, for each structure, calculations were performed with the bridging Cys residue in both its protonated and deprotonated forms (Table 2).[62] Only the $[Fe-Fe]^{3+}$ oxidation state of the $[2Fe]_H$ component was considered for these truncated H-cluster models because the $[Fe-Fe]^{5+}$ state was deemed implausible on the basis of the computational results discussed above.

The MO descriptions provided by DFT for the **H$_{ox}$** and **H$_{ox}$-CO** states of the $[2Fe]_H$ component can be rationalized with straightforward ligand-field arguments. In the both states, the Fe_p and Fe_d centers possess distorted octahedral or square-pyramidal coordination environments that (to a first approximation) split the Fe d-based MOs into "e_g" and "t_{2g}" sets (Figure 2, top). Extensive metal−metal bonding interactions ensure that these Fe-based MOs are delocalized, to varying degrees, over the entire $[2Fe]_H$ dimer. The six Fe d-based MOs constituting the t_{2g} set are fully occupied, consistent with both Fe centers being LS. These MOs exhibit substantial contributions (~20%) from the terminal CO/CN ligands due to strong π-back-bonding interactions. In the paramagnetic **H$_{ox}$** and **H$_{ox}$-CO** states, the lone unpaired electron occupies a MO derived from one or both of the z^2 orbitals of the Fe centers, along with a variable contribution from the π*-acceptor orbital of the CO_b ligand oriented in the $Fe-C(O)_b-Fe$ plane (Figure 2).[63] As the character of this SOMO is critical for understanding the reactivity and magnetic properties of the cluster, we employed the natural orbital approach[64] to obtain a more intuitive picture of the open-shell wave function. The resulting "magnetic orbitals" and their compositions are displayed in Figure 2 and Table 4, respectively.

Table 4. DFT-Computed Compositions of SOMOs and Mulliken Spin Populations of H-Cluster Models

		SOMO orbital composition (%)					
state	model	Fe_p[a]	Fe_d[a]	Fe_{tot}	S_{Cys}[b]	S_{pdt}[b]	CO/CN[c]
H$_{ox}$	**ox^{SH}**	5.0	79.2	84.2	0.3	4.4	9.2
	ox^{S}	5.7	76.7	82.4	1.0	3.9	10.8
H$_{ox}$-CO	**ox^{SH}-CO**	53.4	14.4	67.8	4.8	6.6	17.8
	ox^{S}-CO	33.6	27.1	60.7	7.2	9.3	20.2

		Mulliken spin populations				
state	model	Fe_p	Fe_d	S_{Cys}	S_{pdt}	CO/CN
H$_{ox}$	**ox^{6Fe}**	0.08	0.86	−0.02	0.05	−0.07
H$_{ox}$-CO	**ox^{6Fe}-CO**	0.41	0.22	0.02	0.10	−0.01

[a] Fe 3d, 4s, and 4p contributions. [b] S 3s, 3p, and 3d contributions. [c] 2s and 2p contributions from the C, N, and O atoms of the CO and CN ligands.

For the two truncated **H$_{ox}$** models, **ox^{SH}** and **ox^{S}**, nearly 80% of the unpaired spin density is localized on the Fe_d center in a z^2-shaped orbital that points toward the vacant coordination site (Figure 2, bottom), while the remainder is delocalized over the adjacent ligands. Only a small fraction (5%) of the spin density appears on the proximal site, and the $[2Fe]_H$ component in the **H$_{ox}$** state is therefore best described as possessing an $Fe_p^{2+}-Fe_d^{+}$ core. This formal oxidation state assignment is consistent with the fact that the five-coordinate Fe_d center is expected to have a higher redox potential than the six-coordinate Fe_p center. As shown in Table 4, the protonation state of the terminal Cys ligand has almost no effect on the composition of the corresponding **H$_{ox}$** SOMO, which in each case contains very little S_{Cys} character.

The addition of CO to the distal site dramatically alters the composition of the SOMO by "pushing" unpaired spin density away from Fe_d and onto Fe_p (Table 4). As shown in Figure 2, the SOMOs of the **ox^{SH}-CO** and **ox^{S}-CO** models are comprised of the antisymmetric combination of z^2-like orbitals of the two Fe centers but also possess a significant

(62) In the **ox^{SH}** and **ox^{SH}-CO** models, the thiol proton was placed along the $S_{Cys}-Fe_1$ bond axis of the corresponding 6Fe model, and the $S_{Cys}-H$ bond distance was fixed at 1.37 Å.

(63) Liu and Hu report a MO diagram for the $[2Fe]_H$ subcluster similar to the one shown in Figure 2, top.[31] Likewise, they also note that the redox-active MO has primarily Fe(e_g) and $CO_b(\pi^*)$ character.

(64) (a) Green, M. T. *J. Am. Chem. Soc.* **2001**, *123*, 9218−9219. (b) Green, M. T. *J. Am. Chem. Soc.* **1999**, *121*, 7939−7940.

contribution from the in-plane π^*-acceptor orbital of the CO_b ligand. Thus, in contrast to the localized nature of the $\mathbf{H_{ox}}$ state, the $\mathbf{H_{ox}}$**-CO** state features a more delocalized wave function, and both Fe centers therefore have formal oxidation states between 1+ and 2+. The extent of spin delocalization is somewhat dependent on the protonation state of the S_{Cys} donor because the weaker-donating thiol ligand of $\mathbf{ox^{SH}}$**-CO** allows for a greater degree of spin localization on Fe_p compared to the anionic thiolate of $\mathbf{ox^{S}}$**-CO**. It is also important to note that, compared to $\mathbf{H_{ox}}$, the amount of Fe character in the $\mathbf{H_{ox}}$**-CO** SOMOs is reduced by nearly 20%, accompanied by large increases in S_{Cys} and CO_b orbital contributions.

Significantly, these electronic structure descriptions provided by DFT offer a rationale for the large increase in J_H upon CO binding to Fe_d. In the $\mathbf{H_{ox}}$ state, the spin density is concentrated on the Fe_d, which lacks an effective exchange pathway to the $[Fe_4S_4]_H$ cluster (Fe_d is located more than 6 Å from the nearest Fe of the cubane). Yet, the large amount of unpaired spin density on Fe_p in the $\mathbf{H_{ox}}$**-CO** state facilitates exchange interactions with the cubane via the bridging Cys residue that carries substantial (~6%) spin density in the $\mathbf{H_{ox}}$**-CO** models. Thus, the delocalization of spin over the Fe dimer induces more paramagnetism into the $[Fe_4S_4]_H$ cluster, in excellent agreement with previous Mössbauer studies.[18,19] It is also important to note that the spin distributions calculated for the $[2Fe]_H$ component are fully consistent with the Mulliken spin populations obtained from calculations on the full H-cluster (Table 4).[65] Indeed, the agreement between the truncated and full models is nearly quantitative for the $\mathbf{H_{ox}}$ state, whereas for the $\mathbf{H_{ox}}$**-CO** state, the spin distribution computed for $\mathbf{ox^{6Fe}}$**-CO** is intermediate between those calculated for $\mathbf{ox^{SH}}$**-CO** and $\mathbf{ox^{S}}$**-CO**. This result suggests that the donor strength of the bridging Cys ligand in the H-cluster is intermediate between a thiol and a thiolate.

4. EPR Parameters. The prediction of EPR parameters by means of electronic structure calculations is an excellent method for validating computational models on the basis of experimental data. To this end, the g values for the $\mathbf{H_{ox}}$ and $\mathbf{H_{ox}}$**-CO** states were computed using two distinct DFT methodologies: (i) relativistic calculations with ZORA,[48] as implemented in ADF, and (ii) the CP-SCF approach,[50] as implemented in ORCA. Additional calculations were performed using the semiempirical INDO/S method,[54] which has been applied successfully to numerous transition-metal complexes.[66] As these three methodologies are not compatible with the BS approach, it was only possible to compute EPR parameters for the $[2Fe]_H$ component (in both its thiol- and thiolate-ligated forms).

As shown in Table 5, all three computational methods provide g values for the $\mathbf{H_{ox}}$ state that are generally consistent with each other and with the experimental data. The INDO/S results are more accurate for g_1 and g_2, whereas the DFT methods correctly predict g_3 to be quite close to the free-electron value of 2.002. Because the composition of the SOMO of the truncated $\mathbf{H_{ox}}$ models is largely independent of the protonation state of S_{Cys} (vide supra), it is not surprising that the calculated g values for $\mathbf{ox^{SH}}$ and $\mathbf{ox^{S}}$ are nearly identical. Importantly, these g-value calculations also provide an independent means by which to distinguish between the competing oxidation states of $\mathbf{H_{ox}}$ (i.e., $[2Fe]_H^{3+}$ vs $[2Fe]_H^{5+}$) because the g values calculated for the $\mathbf{ox^{2Fe-high}}$ model (2.181, 2.098, and 2.008) deviate strongly from the reported values (Table 5), in further support of the lower oxidation state.

Table 5. Comparison of Experimental and Calculated g Values for $[2Fe]_H$ Models of the $\mathbf{H_{ox}}$ and $\mathbf{H_{ox}}$**-CO** States

		g values		
$\mathbf{H_{ox}}$	method[a]	g_1	g_2	g_3
*Cp*I	exp[b]	2.098	2.040	2.001
*Cp*II	exp	2.078	2.027	1.999
*Dv*H	exp	2.100	2.040	2.000
$\mathbf{ox^{SH}}$	ADF (ZORA)	2.071	2.025	2.000
	ORCA (CP-SCF)	2.082	2.028	2.014
	INDO/S-CI	2.095	2.055	2.030
$\mathbf{ox^{S}}$	ADF (ZORA)	2.065	2.030	2.015
	ORCA (CP-SCF)	2.085	2.035	2.012
	INDO/S-CI	2.097	2.053	2.020
		g values		
$\mathbf{H_{ox}}$**-CO**	method[a]	g_1	g_2	g_3
*Cp*I	exp[b]	2.074	2.011	2.011
*Cp*II	exp	2.032	2.017	1.988
*Dv*H	exp	2.060	2.010	2.010
$\mathbf{ox^{SH}}$**-CO**	ADF (ZORA)	2.025	2.016	2.002
	ORCA (CP-SCF)	2.032	2.020	2.009
	INDO/S-CI	2.078	2.063	2.012
$\mathbf{ox^{S}}$**-CO**	ADF (ZORA)	2.009	2.002	1.990
	ORCA (CP-SCF)	2.012	2.008	1.995
	INDO/S-CI	2.053	2.036	2.007

[a] See the Computational Details section for more information regarding the methods used to calculate g values. [b] See Table 1 for references for experimental values.

The interpretation of the computed g values for the $\mathbf{H_{ox}}$**-CO** state is less straightforward for two reasons. First, the two FeHases isolated from *Cp* yield very different sets of g values when treated with CO (Tables 1 and 5), complicating the comparison of experimental and computed data. While the small, rhombic g values predicted by DFT calculations for the $\mathbf{ox^{SH}}$**-CO** model agree nicely with those reported for the *Cp*II H-cluster, all three techniques fail to reproduce the axial EPR signals exhibited by *Cp*I and *Dv*H (Table 5). Although the INDO/S method yields a fairly axial **g** tensor with a g_1 value near the experimental *Cp*I and *Dv*H values of ~2.07, it incorrectly predicts $g_\perp > g_\parallel$, suggesting that this method fails to generate a proper description of the SOMO. Second, the protonation state of S_{Cys} has a large impact on the computed g values for the $\mathbf{H_{ox}}$**-CO** state, with all three techniques showing sizable decreases in g shifts upon thiol deprotonation. This trend is understood by the fact that the SOMO of the $\mathbf{ox^{SH}}$**-CO** model is more localized (on Fe_p) and less covalent than that of $\mathbf{ox^{S}}$**-CO**, factors that are expected to produce larger g shifts for the former model. Significantly, the agreement between experimental and

(65) For a system with $S = {}^1/_2$, the Mulliken spin for a given atom (multiplied by 100) should be approximately equal to its percent contribution to the SOMO.

(66) Neese, F.; Solomon, E. I. *Inorg. Chem.* **1998**, *37*, 6568−6582.

Table 6. Comparison of Experimental and DFT-Calculated ^{13}C Hyperfine Coupling Constants (A^C) for the Exogenous CO Ligand of the H-Cluster in the **H_{ox}-CO** State

		^{13}C A^C values (MHz)			
H_{ox}-CO	method[a]	A^C_{11}	A^C_{22}	A^C_{33}	A^C_{iso}
*Cp*I	exp[b]	+22	+20	+20	+21
*Cp*II	exp	+36	+34	+29	+33
ox^{SH}-CO	ADF	+49	+44	+42	+45
	ORCA	+35	+28	+25	+29
ox^{S}-CO	ADF	+74	+67	+65	+68
	ORCA	+62	+50	+46	+53

[a] See the Computational Details section for more information regarding the methods used to calculate hyperfine coupling constants. [b] Experimental values obtained from ref 15.

computed g values is far superior for **ox^{SH}-CO** than **ox^{S}-CO**, indicating that the former model better reproduces the electronic structure of the $[2Fe]_H$ component in the actual H-cluster (i.e., with the $[Fe_4S_4]_H$ cubane present).

We also used the two distinct DFT methods to calculate the ^{13}C hyperfine coupling constants (A^C) for the *added* CO ligand, a parameter that has been measured experimentally with ENDOR spectroscopy for both *Cp*I and *Cp*II.[15] In agreement with the spectroscopic data, both methods predict relatively isotropic $\mathbf{A}^C$ tensors, although the ZORA method yields A^C values that are uniformly greater by ~15 MHz (Table 6).[67] Because the calculated isotropic A^C values (A^C_{iso}) for the **ox^{SH}-CO** and **ox^{S}-CO** models roughly reflect the amount of spin density on the Fe_d center, the A^C parameter provides a qualitative measure of the spin distribution within the **H_{ox}-CO** state. As with the DFT-computed **g** tensors, the **ox^{SH}-CO** model yields A^C values that are closer to the experimental values for *Cp*II than those obtained for **ox^{S}-CO**, providing further evidence that this computational model more accurately reproduces the electronic structure of the $[2Fe]_H$ component of the *Cp*II H-cluster. Consequently, we can conclude that the $[2Fe]_H$ component in the **H_{ox}-CO** state of *Cp*II, like the **ox^{SH}-CO** model, is better described as possessing a valence-localized $[Fe_p^{+}-Fe_d^{2+}]$ core rather than a delocalized $[Fe_p^{1.5+}-Fe_d^{1.5+}]$ core. Notably, the A^C_{iso} value of 21 MHz for *Cp*I is substantially smaller than the *Cp*II value of 34 MHz (Table 6), suggesting that the $[2Fe]_H$ cluster in the former enzyme is even closer to the localized limit $[Fe_p^{+}-Fe_d^{2+}]$. This difference in delocalization would also explain the larger g shifts of *Cp*I compared to *Cp*II, as well as the larger ^{57}Fe hyperfine coupling constants measured for the $[Fe_4S_4]_H$ cluster of *Cp*I (Table 1).

Mössbauer[18,19] and ^{57}Fe ENDOR[15,16] studies of FeHases have revealed isotropic Fe **A** tensors for the $[2Fe]_H$ component in both the **H_{ox}** and **H_{ox}-CO** states (Table 7). Many researchers have noted that this result is quite perplexing because LS Fe^{+} (and Fe^{3+}) centers are expected to yield anisotropic **A** tensors via spin dipolar interactions.[19] Indeed, our DFT calculations support this theoretical prediction, providing hyperfine coupling constants for the (paramagnetic)

Table 7. Comparison of Experimental and DFT-Calculated ^{57}Fe Hyperfine Values for the **H_{ox}** and **H_{ox}-CO** States

			^{57}Fe A values (MHz)			
H_{ox}	method[a]	Fe site	A_{11}	A_{22}	A_{33}	A_{iso}
*Cp*II	exp[b]	$[2Fe]_H$	−18.0	−18.0	−18.0	−18.0
*Dv*H	exp		−12.0	−12.0	−12.0	−12.0
ox^{SH}	ADF	Fe_d	+11.0	−1.0	−27.5	−5.8
	ORCA		+14.1	−7.2	−43.8	−12.3
ox^{S}	ADF	Fe_d	+12.1	−2.3	−23.0	−4.4
	ORCA		+16.8	−7.9	−36.4	−9.2
			^{57}Fe A values (MHz)			
H_{ox}-CO	method[a]	Fe site	A_{11}	A_{22}	A_{33}	A_{iso}
*Cp*II	exp[b]	$[2Fe]_H$	−9.5	−9.5	−9.5	−9.5
*Dv*H	exp		−5.0	−5.0	−5.0	−5.0
ox^{SH}-CO	ADF	Fe_p	+26.4	−0.6	−3.2	+7.5
	ORCA		+29.5	−0.3	−8.3	+7.0
ox^{S}-CO	ADF	Fe_p	+16.5	−5.8	−7.4	+1.1
	ORCA		+18.1	−6.6	−11.0	+0.2

[a] See the Computational Details section for more information regarding the methods used to calculate hyperfine coupling constants. [b] See Table 1 for references for experimental values.

Fe_d center of **ox^{SH}** and **ox^{S}** that are decidedly anisotropic and thus in poor agreement with the experimental data, although the ORCA method does yield reasonable values for A_{iso} (Table 7).[68] This discrepancy is not resolved by using a more oxidized $[Fe-Fe]^{5+}$ core for the **H_{ox}** state, as DFT computations on **$ox^{2Fe-high}$** result in a highly anisotropic **A** tensor for the paramagnetic Fe_p^{3+} center (Table S3). Similarly, the **A** tensors computed for the Fe_p centers of the **ox^{SH}-CO** and **ox^{S}-CO** models are quite anisotropic; however, our calculations, nonetheless, reproduce the overall decrease in magnitude of A_{iso} upon the addition of CO.

Our DFT calculations thus offer little insight into the origin of the isotropic ^{57}Fe hyperfine values of the $[2Fe]_H$ component. This shortcoming is made more surprising by the fact that DFT computations on our $[2Fe]_H$ models are quite capable of reproducing the experimental g values and ligand hyperfine coupling constants reported for **H_{ox}** and **H_{ox}-CO**, suggesting that the overall electronic wave function is reasonable. It is also interesting to note that the ADF and ORCA approaches, which utilize distinct means of calculating hyperfine values, provide **A** tensors that are largely consistent with each other, indicating that the problem is not limited to a particular methodology. As previous DFT studies of mononuclear Fe complexes have had success in predicting ^{57}Fe hyperfine coupling constants,[50b] the shortcomings described herein may be due to the binuclear structure of the $[2Fe]_H$ component. For instance, despite the localized nature of the **H_{ox}** state as revealed by our computed MO description and the experimental observation that hyperfine coupling involves a single Fe center within the $[2Fe]_H$ component, our computational results indicate that the single unpaired electron is magnetically coupled to both Fe centers,

(67) This discrepancy between ADF and ORCA computations is likely due to the fact that the former utilized the nonhybrid BP functional, whereas the latter used the hybrid B3LYP functional. It is well-known that nonhybrid functionals tend to overestimate the degree of metal−ligand covalency, generally leading to larger ligand hyperfine values.

(68) A recent report by Neese and co-workers suggested scaling factors of 1.69−1.81 for the isotropic component of the **A** tensor.[50d] Although such an adjustment may, in some instances, improve the agreement of our computed A_{iso} values with the experimental results, it does not account for the large anisotropies of the calculated **A** tensors.

although the calculated A values for Fe_p are significantly smaller in magnitude than those for Fe_d (Table S3).

Discussion

The computational study described here is the first to incorporate the $[Fe_4S_4]_H$ cluster in its models of the H-cluster, and this approach has yielded previously unattainable insights into the geometric and electronic structures of this unique active site. Using a BS methodology, DFT has provided accurate geometries of the full H-cluster in its $\mathbf{H_{ox}}$ and $\mathbf{H_{ox}}$-**CO** states and also permitted a quantitative analysis of the exchange interactions that exist within the H-cluster. Comparison to the smaller 2Fe model (**ox^{2Fe}**) suggests that the presence of the $[Fe_4S_4]_H^{2+}$ cluster lengthens the bond between Fe_p and the bridging S_{Cys} ligand, which, in turn, strongly influences the position of the CO_b ligand relative to the $[2Fe]_H$ core. Because the π*-acceptor orbital of CO_b contributes to the Fe-based MO carrying the unpaired electron, this indirect influence of the cubane likely adjusts the redox potentials of the various H-cluster oxidation states. Significantly, attempts to model the full H-cluster in the other potential $\mathbf{H_{ox}}$ oxidation state of $[Fe_p-Fe_d]^{5+}$ failed to produce the correct metal valencies and active-site geometry, thereby providing strong evidence that such higher oxidation states of the binuclear site are not feasible in the presence of the $[Fe_4S_4]_H^{2+}$ cubane.

The results obtained in these studies also permit us to rationalize many of the spectroscopic features of the H-cluster on the basis of the corresponding electronic structures. Specifically, our results indicate that the $[2Fe]_H$ component in the $\mathbf{H_{ox}}$ state possesses a valence-localized $Fe_p^{2+}-Fe_d^{+}$ core, whereas in the $\mathbf{H_{ox}}$-**CO** state, it exhibits significant valence delocalization, with both Fe centers carrying significant spin density. This change is reflected experimentally in the increase in J_H by nearly an order of magnitude upon binding of CO to Fe_d, a result that is accurately reproduced by our BS calculations.

Taking advantage of recent advances in DFT, we were also able to perform the first calculations of EPR parameters for the $[2Fe]_H$ subunit. All three methodologies employed, including the DFT-based ZORA and CP-SCF approaches and the semiempirical INDO/S-CI method, yield accurate g values for the valence-localized $\mathbf{H_{ox}}$ state, while those computed by DFT for the $\mathbf{H_{ox}}$-**CO** state are most consistent with the rhombic spectrum of the *Cp*II enzyme, but not with the axial signals of *Cp*I and *Dv*H. The decrease in g shifts from $\mathbf{H_{ox}}$ and $\mathbf{H_{ox}}$-**CO** directly reflects the increased delocalization and ligand orbital character of the SOMO in the latter state. Similarly, the ^{13}C hyperfine values for the exogenous CO ligand of Fe_d are sensitive reporters of the spin distribution within the $\mathbf{H_{ox}}$-**CO** state, with smaller A^C_{iso} values indicative of decreased spin density on the Fe_d center, and hence greater spin localization onto Fe_p. Thus, we have identified several parameters (J_H, g shifts, and ^{13}C A^C values) that are diagnostic of the electronic structure of the $[2Fe]_H$ component. However, our success in predicting reasonably accurate g values and ligand hyperfine tensors was not matched by the corresponding metal hyperfine calculations, which do not provide the isotropic ^{57}Fe **A** tensor of the binuclear site found experimentally. Given the unique electronic properties of the binuclear $[2Fe]_H$ component, along with the fact that current methods for calculating EPR parameters cannot explicitly treat the $[Fe_4S_4]_H$ cubane, this discrepancy between experimental and computed metal hyperfine parameters is perhaps not surprising.

Scheme 1. Proposed Structures of the $\mathbf{H_{ox}^{photo}}$ State of the H-Cluster[22]

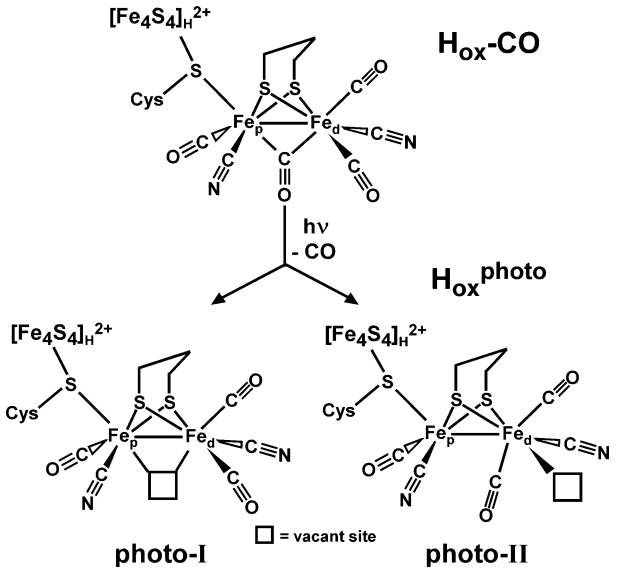

Models of the $\mathbf{H_{ox}^{photo}}$ State. As demonstrated above, our computational methodology is capable of providing viable geometric and electronic structure descriptions and, in many instances, reasonably accurate spectral parameters for the H-cluster. Consequently, we can confidently extend this methodology to the $\mathbf{H_{ox}^{photo}}$ state, for which only limited structural and spectroscopic data are available. This species, which is generated by irradiation of the $\mathbf{H_{ox}}$-**CO** state at cryogenic temperatures, is characterized by a highly rhombic EPR spectrum with $g = 2.26$, 2.12, and 1.89.[14] Moreover, detailed IR studies by Bagley and co-workers[22] have demonstrated that the $\mathbf{H_{ox}^{photo}}$ species lacks the bridging CO ligand found for the $\mathbf{H_{ox}}$ and $\mathbf{H_{ox}}$-**CO** states; hence, two structures were proposed for this species (Scheme 1): the **photo-I** structure, generated by direct dissociation of the CO_b ligand, and **photo-II**, obtained by dissociation of the terminal CO ligand of Fe_d followed by migration of CO_b to a terminal position. The $[2Fe]_H$ component likely remains in the $[Fe-Fe]^{3+}$ state upon conversion of $\mathbf{H_{ox}}$-**CO** to $\mathbf{H_{ox}^{photo}}$ because two-electron oxidation would result in substantial increases in the energies of the ν(CO) modes. Instead, these frequencies actually decrease in energy upon photolysis, which was attributed to the loss of a π-accepting CO ligand.[22]

Building upon the experimental foundation established by Bagley and co-workers, 6Fe models of **photo-I** and **-II** were generated from the **ox^{6Fe}-CO** model by removal of the appropriate CO ligand. Subsequent DFT geometry optimizations of these models resulted in the **I^{6Fe}** and **II^{6Fe}** structures shown in Figure 3. In the **I^{6Fe}** model, both Fe centers of the $[2Fe]_H$ component adopt distorted square-pyramidal coordination environments, and the overall structure closely

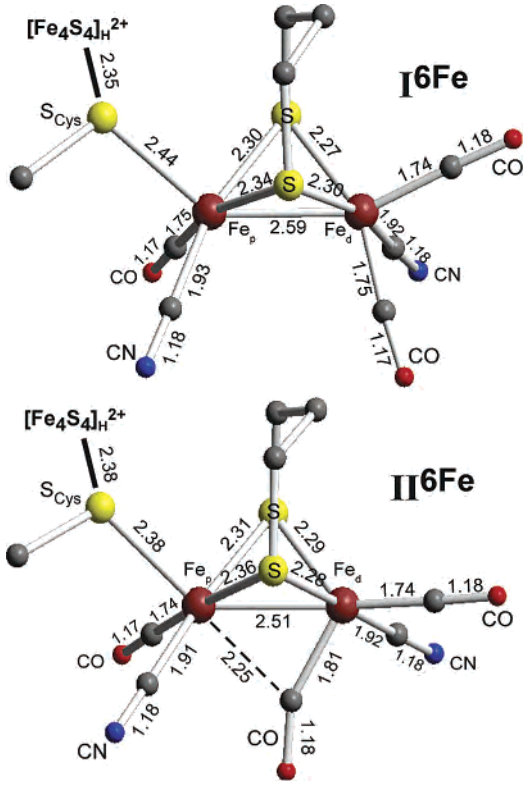

Figure 3. DFT-optimized structures of the $\mathbf{I}^{\mathbf{6Fe}}$ and $\mathbf{II}^{\mathbf{6Fe}}$ models of the $\mathbf{H_{ox}}^{\mathbf{photo}}$ state with relevant bond distances shown in angstroms. The $[Fe_4S_4]_H^{2+}$ cluster has been omitted for the sake of clarity.

resembles that of many synthetic FeHase model complexes also lacking a CO_b ligand.[27] However, because of the presence of the $[Fe_4S_4]_H^{2+}$ cubane, the Fe_p-S_{Cys} distance of 2.44 Å in $\mathbf{I}^{\mathbf{6Fe}}$ is significantly longer than the corresponding bond lengths observed in the synthetic $[2Fe]_H$ model complexes of Pickett and co-workers (~2.25 Å).[69] For the $\mathbf{II}^{\mathbf{6Fe}}$ model, removal of the terminal CO ligand of Fe_d does indeed shift the bridging CO_b ligand toward the distal center, but the position of CO_b is better described as semibridging, not terminal. Thus, the $\mathbf{II}^{\mathbf{6Fe}}$ structure appears less consistent with the vibrational data available for $\mathbf{H_{ox}}^{\mathbf{photo}}$ than $\mathbf{I}^{\mathbf{6Fe}}$. Moreover, the $\mathbf{I}^{\mathbf{6Fe}}$ model is more stable than $\mathbf{II}^{\mathbf{6Fe}}$ by >10 kcal/mol, indicating that the latter lies in a local energy minimum. Indeed, upon further optimization with very stringent convergence criteria, the $\mathbf{II}^{\mathbf{6Fe}}$ structure spontaneously converted to $\mathbf{I}^{\mathbf{6Fe}}$.

Following the same procedure utilized above for the $\mathbf{H_{ox}}$ and $\mathbf{H_{ox}}$-**CO** states, the electronic and magnetic properties of the putative $\mathbf{H_{ox}}^{\mathbf{photo}}$ models, $\mathbf{I}^{\mathbf{6Fe}}$ and $\mathbf{II}^{\mathbf{6Fe}}$, were further examined with calculations on the corresponding $[2Fe]_H$ components, where the $[Fe_4S_4]_H$ cubane was replaced by a proton. As shown in Figure 4, the unpaired electrons of these truncated models, termed $\mathbf{I}^{\mathbf{SH}}$ and $\mathbf{II}^{\mathbf{SH}}$, are largely localized on the Fe_p and Fe_d centers, respectively, and in each case the SOMO contains ≥80% Fe d orbital character. Thus, the $[2Fe]_H$ components of $\mathbf{I}^{\mathbf{SH}}$ and $\mathbf{II}^{\mathbf{SH}}$ can be described as posessing $[Fe_p^{+}-Fe_d^{2+}]$ and $[Fe_p^{2+}-Fe_d^{+}]$ cores, respectively,

(69) Razavet, M.; Davies, S. C.; Hughes, D. L.; Barclay, J. E.; Evans, D. J.; Fairhurst, S. A.; Liu, X. M.; Pickett, C. J. *J. Chem. Soc., Dalton Trans.* **2003**, 586−595.

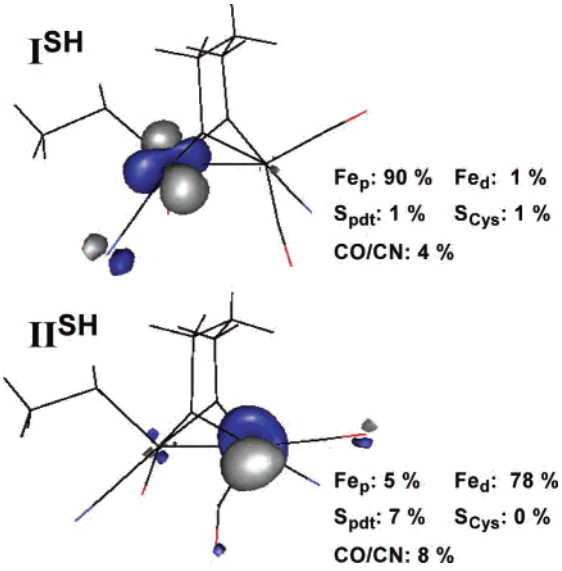

Figure 4. Isosurface plots of the SOMOs obtained from spin-unrestricted DFT computations on the $\mathbf{I}^{\mathbf{SH}}$ (top) and $\mathbf{II}^{\mathbf{SH}}$ (bottom) models. The computed MO compositions are shown to the right. The $[2Fe]_H$ components are oriented as in Figure 2.

Table 8. Computed Magnetic Parameters for DFT-Optimized Models of the $\mathbf{H_{ox}}^{\mathbf{photo}}$ State and Comparison to Experimental Data

		g values			
$\mathbf{H_{ox}}^{\mathbf{photo}}$	method[a]	g_1	g_2	g_3	^{13}C A_{iso} value (MHz)
*Cp*I	exp[b]	2.260	2.120	1.890	N/A[c]
$\mathbf{I}^{\mathbf{SH}}$	**ADF**[d]	**2.380**	**2.158**	**1.996**	−8.5
	ORCA	2.112	2.066	2.026	−19.1
	INDO/S-CI[d]	**2.189**	**2.127**	**2.027**	
$\mathbf{II}^{\mathbf{SH}}$	ADF	2.105	2.070	2.014	−18.5
	ORCA	2.135	2.083	2.021	−29.8
	INDO/S-CI	2.120	2.090	2.020	

[a] See the Computational Details section for more information regarding the methods used to calculate *g* values and hyperfine coupling constants. [b] See Table 1 for references for experimental values. [c] N/A = not available. [d] Computed values that are in particularly good agreement with the experimental data are in boldface.

in full agreement with the Mulliken spin populations calculated for the corresponding 6Fe models. Additionally, both SOMOs possess z^2-like orbital shapes that are pointed toward the vacancies originally occupied by the dissociated CO ligands.

Table 8 shows the *g* values calculated for the $\mathbf{H_{ox}}^{\mathbf{photo}}$ models with the DFT-based ZORA and CP-SCF approaches, as well as the INDO/S-CI method, along with the ^{13}C A_{iso} values computed for the exogenous CO ligand. All three computational schemes provide similar *g* values for the $\mathbf{II}^{\mathbf{SH}}$ model (~2.12, 2.08, and 2.02) that are inconsistent with the large rhombic values reported for $\mathbf{H_{ox}}^{\mathbf{photo}}$. On the other hand, for reasons that are not clear, the computed *g* values for $\mathbf{I}^{\mathbf{SH}}$ vary greatly from one method to another (Table 8). Specifically, while the CP-SCF method provides similar sets of *g* values for both models, the ZORA and INDO/S methods predict considerably larger *g* shifts with substantial rhombicity for the $\mathbf{I}^{\mathbf{SH}}$ model. These latter results, which are highlighted in Table 8, are reasonably consistent with the experimental data, although the agreement is not quantitative. Therefore, while our computational results are somewhat

ambiguous, it appears that the $\mathbf{I^{SH}}$ model better reproduces the rhombic EPR spectrum of the $\mathbf{H_{ox}^{photo}}$ intermediate.

The vastly different magnitudes of the *g* shifts predicted for $\mathbf{I^{SH}}$ and $\mathbf{II^{SH}}$ are easily rationalized on the basis of the corresponding electronic structures. In the case of $\mathbf{I^{SH}}$, the unpaired electron occupies the Fe_p z^2-based MO that is oriented along the Fe_p-S_{Cys} bond vector (Figure 4). The presence of the $[Fe_4S_4]_H$ cluster elongates this "axial" bond to 2.44 Å, resulting in an almost four-coordinate (square-planar) environment for the Fe_p center. Importantly, this coordination geometry stabilizes the Fe_p-based SOMO of $\mathbf{I^{SH}}$, bringing it in close energetic proximity to the filled Fe d-based MOs and thus permitting the ground-state wave function to acquire substantial orbital angular momentum (via SOC with low-lying electronic excited states) that leads to a large **g**-tensor anisotropy. In contrast, in $\mathbf{II^{SH}}$, the unpaired spin density is located on the five-coordinate Fe_d center. This coordination geometry, along with the presence of an additional semibridging CO ligand, gives rise to a large energy splitting between the SOMO and the filled t_{2g} set of MOs. The $\mathbf{II^{SH}}$ model is therefore expected to yield smaller *g* shifts than $\mathbf{I^{SH}}$, in agreement with our computational data. Although the ^{13}C hyperfine values for the exogenous CO ligand of $\mathbf{H_{ox}^{photo}}$ have not yet been measured experimentally, our computational results in Table 8 suggest that these values could aid in further distinguishing between the **photo-I** and **-II** structures. On the basis of the ORCA results, which proved more accurate for the $\mathbf{H_{ox}}$**-CO** state, values of $|A_{iso}|$ near ~20 and 30 MHz would be characteristic of the **photo-I** and **-II** structures, respectively. Moreover, with the relative spin distributions of the $\mathbf{I^{SH}}$ and $\mathbf{II^{SH}}$ models noted above, we would expect the **photo-I** structure to give rise to a more sizable J_H value and larger ^{57}Fe *A* values for its $[Fe_4S_4]_H^{2+}$ cluster than the **photo-II** structure. Hence, our results suggest that Mössbauer spectroscopy should provide a particularly powerful tool to distinguish between viable $\mathbf{H_{ox}^{photo}}$ models.

Given the greater stability of the $\mathbf{I^{6Fe}}$ model compared to the $\mathbf{II^{6Fe}}$ model, along with the fact that the former yields calculated *g* values that appear more consistent with experimental EPR data, we favor the **photo-I** structure for the $\mathbf{H_{ox}^{photo}}$ state. This conclusion is corroborated by the work of synthetic chemists, who have had difficulties generating FeHase model complexes with a bridging CO ligand, suggesting that such entities are inherently unstable.[70,71] Although the structural basis for the stability of the $[Fe_p-CO_b-Fe_d]_H$ core in the enzyme remains unknown, the results obtained in this and previous[31,72] computational studies clearly indicate that this positioning of a CO ligand between the two Fe centers has a dramatic effect on the electronic structure, and thus the reactivity, of the remarkably complex H-cluster.

Acknowledgment. This research was supported by funds from the University of Wisconsin and the Sloan Foundation Research Fellowship Program (T.C.B.) and the NSF Graduate Research Fellowship Program (A.T.F.). We thank Dr. Frank Neese (MPI Mülheim) for providing a free copy of ORCA and for useful discussions and comments.

Supporting Information Available: Structural parameters for the $\mathbf{ox^{6Fe-high}}$ and $\mathbf{ox^{2Fe-high}}$ models (Table S1), calculated exchange parameters (Table S2), complete ^{57}Fe **A** tensors for several models (Table S3), and Cartesian coordinates for all DFT geometry-optimized models (Table S4a−g). This material is available free of charge via the Internet at http://pubs.acs.org.

IC050946F

(70) Although the incorporation of a bridging CO ligand into FeHase models has proved quite challenging, complexes with this feature were recently synthesized and characterized by Rauchfuss and co-workers. See ref 71.

(71) Boyke, C. A.; Rauchfuss, T. B.; Wilson, S. R.; Rohmer, M. M.; Benard, M. *J. Am. Chem. Soc.* **2004**, *126*, 15151−15160.

(72) (a) Darensbourg, M. Y.; Lyon, E. J.; Zhao, X.; Georgakaki, I. P. *Proc. Natl. Acad. Sci. U.S.A.* **2003**, *100*, 3683−3688. (b) Fiedler, A. T.; Brunold, T. C. *Inorg. Chem.* **2005**, *44*, 1794−1809.